IEEE Photonics Journal
An IEEE Photonics Society Publication

Open Access

Silicon-on-Insulator Waveguide Devices for Broadband Mid-Infrared Photonics

Volume 9, Number 3, June 2017

Bowei Dong
Xin Guo
Chong Pei Ho
Bo Li
Hong Wang
Chengkuo Lee
Xianshu Luo
Guo-Qiang Lo

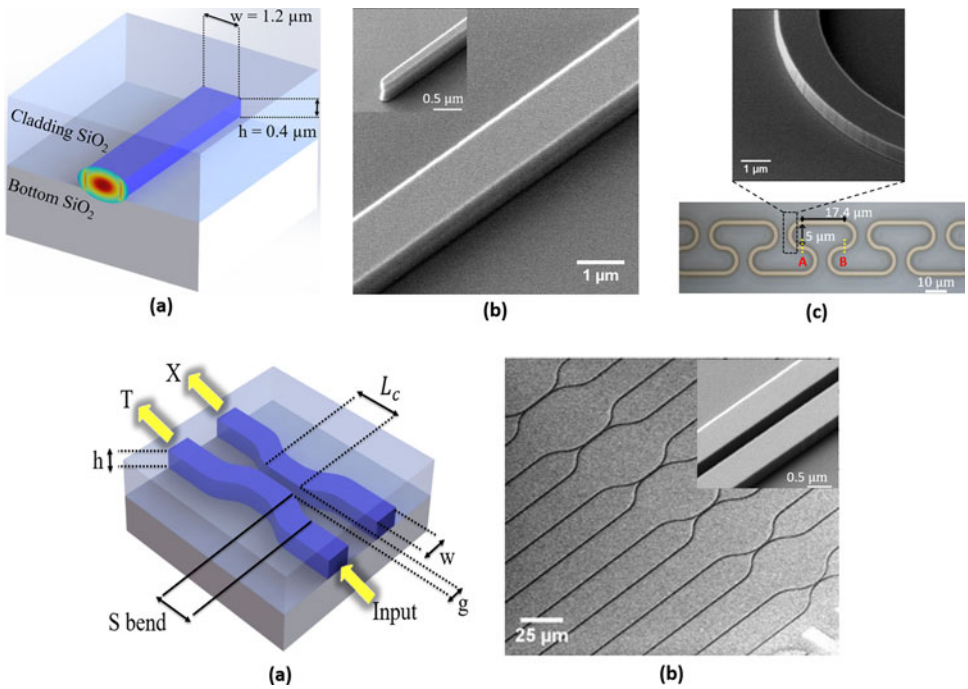

DOI: 10.1109/JPHOT.2017.2692039
1943-0655 © 2017 IEEE

IEEE photonics SOCIETY

IEEE

Silicon-on-Insulator Waveguide Devices for Broadband Mid-Infrared Photonics

Bowei Dong,[1,2,3] Xin Guo,[4] Chong Pei Ho,[2] Bo Li,[2] Hong Wang,[4] Chengkuo Lee,[2,3] Xianshu Luo,[1] and Guo-Qiang Lo[1]

[1]Institute of Microelectronics, Agency for Science, Technology and Research (A*STAR), Innovis, Singapore 138634
[2]Department of Electrical and Computer Engineering, National University of Singapore, Singapore 117583
[3]NUS Graduate School for Integrative Sciences and Engineering, Centre for Life Science, Singapore 117456
[4]School of Electrical & Electronic Engineering, Nanyang Technological University, Singapore 639798

DOI:10.1109/JPHOT.2017.2692039

Manuscript received March 17, 2017; revised April 3, 2017; accepted April 4, 2017. Date of current version May 4, 2017. Corresponding authors: Chengkuo Lee and Xianshu Luo (e-mail: elelc@nus.edu.sg; luox@ime.a-star.edu.sg).

Abstract: In this paper, we demonstrate silicon-on-insulator (SOI) channel waveguides with propagation loss and $r = 10$ μm bends with bending loss as low as 2 dB/cm and 0.02 dB/90° in the broad wavelength range of 3.68–3.88 μm. We also indicate the limitation of SOI waveguide loss in mid-infrared wavelength by analyzing loss mechanisms. Based on this high-performance mid-infrared waveguide, we systematically analyze the coupling efficiency of various directional couplers, which are critical and commonly used building blocks for on-chip light routing and power splitting. By varying coupling length and sweeping wavelength, the performance of directional coupler with various gap separations is meticulously investigated in 3.68–3.88 μm. A experimental database for directional coupler with any power splitting ratio is provided. Our results offer a promising broadband platform for dense wavelength division multiplexing (DWDM) and applications that require precise control of coupling such as racetrack resonator in the mid-infrared region.

Index Terms: Integrated optics materials, waveguides, mid infrared, photonic integrated circuits.

1. Introduction

"Internet of things (IoT)" is a concept many developed countries are striving for where physical devices are equipped with tiny electronic devices to exchange information to realize a more integrated and efficient society. Sensing is a major aspect as it provides in-situ real time environment detection and monitoring [1]–[6]. Mid-infrared photonics have emerged as a prominent solution for sensing and attracted abundant research interests in recent years because the fingerprints of many common chemical bonds, such as C-H,C=C,O-H, are in the mid-infrared region [7]. With active research effort, environmental [8], [9] and bio-chemical sensing [10]–[12] have already shown promising performance by utilizing mid-infrared photonics. Various materials, including silicon-on-insulator (SOI), silicon-on-sapphire (SOS), silicon nitride (Si_3N_4), aluminum nitride (AlN) and germanium

(Ge), have been demonstrated to achieve mid-infrared photonic devices with low loss and favorable performance [13]–[19].

Among these materials, SOI is undoubtedly the most popular material owing to its fabrication maturity and stability. While previous studies showed the low loss transmission for SOI is limited up to 3.6 μm [20], [21], recent research have confirmed that SOI remains a promising candidate up to 3.8 μm due to the high optical mode confinement enabled by the high refractive index contrast between Si and SiO_2. At 3.8 m, low propagation loss of 1.28 dB/cm, 1.46 dB/cm, and 1.4 dB/cm have been achieved in channel waveguide using 500 nm thick Si core, in rib waveguide using 400 nm thick Si core with 220 nm etch depth, and in slot waveguide with 78 nm gap and 650 nm conductor width respectively [13], [22], [23]. Mach-Zehnder interferometer (MZI) has been demonstrated with a maximum extinction ratio of 34 dB and free-spectral range (FSR) around 10 nm [22]. Multimode interference splitter (MMI) has been designed to provide loss as low as 0.151 dB/MMI [13]. Racetrack resonator with radius $r = 100$ μm and coupling length $L_c = 50$ μm has been reported with a quality factor (Q) of 8200, extinction ratio up to 10 dB, and FSR around 4.12 nm [24]. The success of all these fundamental building blocks envisions a bright future for SOI based mid-infrared photonics applications.

Nevertheless, the wavelength dependence of propagation loss and bending loss in the mid-infrared region lacks investigation. Understanding this dependence is crucial since a spectrum (continuous or broadband wavelength) is usually necessary to meet the various chemical bonds for sensing. Furthermore, though bends with low bending loss have been achieved, its large dimension ($r = 100$ μm) impedes the growing demand of dense integration. Meanwhile, the limitation of SOI waveguide loss mainly caused by silicon oxide absorption needs to be thoroughly studied and understood. Furthermore, directional coupler, as an essential building block in realizing MZI, racetrack resonator, power splitter, and various applications rooted in evanescent wave coupling, needs to be systematically examined in the mid-infrared region.

In this paper, we first study the wavelength dependence of SOI channel waveguide propagation loss and bending loss in the broad wavelength range of 3.68–3.88 μm. This wavelength range gains particular interests due to its coverage of the fingerprints of carcinogenic gas Formaldehyde (CH_2O), toxic Hydrobromic acid (HBr), corrosive Hydrochloric acid (HCl), and biologically crucial glucose ($C_6H_{12}O_6$), providing an ideal sensing window for these chemicals since it avoids the strong water absorption peak in 2.7–3.5 μm. Based on the satisfactory optical loss results, we investigate SOI channel waveguide directional couplers for broadband mid-infrared photonics application. The identically designed devices in three randomly selected chips located in an 8-inch SOI wafer are characterized to reduce the random error. The dependence of directional coupler on both wavelength λ and coupling length L_c is thoroughly studied and analyzed, offering an experimental database for directional coupler with any power splitting ratio. Our demonstrations reveal low optical loss and enable evanescent coupling in broadband integrated mid-infrared photonics. This design can be adopted in on-chip routing, power splitting, and dense wavelength division multiplexing (DWDM) for mid-infrared photonics applications.

2. Channel Waveguides and Bends

The device fabrication starts from a commercially available 8-inch SOI wafer with 220 nm top silicon layer and 3 μm buried oxide (BOX) layer [25], [26]. First, blanket silicon epitaxy is performed in order to increase the top silicon thickness to 400 nm. Silicon dioxide is then deposited as the hard mask for structure definition. The device is patterned by deep ultra-violet (DUV) photolithography followed by a single-step Si reactive ion etching (RIE) to define the waveguide devices. 3 μm SiO_2 is deposited using plasma enhanced chemical vapour deposition (PECVD) as the cladding. Finally, deep trench is formed in order for butt fiber coupling.

The SOI channel waveguide is designed with the dimension of $w \times h = 1.2 \times 0.4$ μm^2 in order to ensure a good optical mode confinement and the single mode condition (see Fig. 1(a)). Fig. 1(b) shows the scanning electron microscope (SEM) image of the fabricated channel waveguide, while the insert shows the SEM image of the inverse waveguide tip for light butt coupling. Waveguide

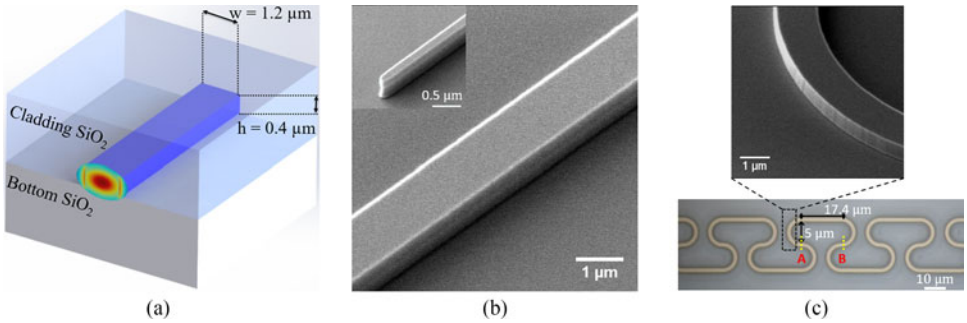

Fig. 1. (a) Schematic of the designed single mode SOI channel waveguide with the dimension of $w \times h = 1.2 \times 0.4\ \mu m^2$. The single-mode profile simulated by COMSOL Multiphysics [27] is shown. (b) SEM image of the straight waveguide. (inset) Inverse taper tip with $w = 0.2\ \mu m$ used for both output and input for light butt coupling. The length of taper is 200 μm. (c) Optical image of $r = 5\ \mu m$ waveguide bends and the SEM image of the bending region. A Fabry-Perot cavity of length 48.8 μm is formed between interface A and B.

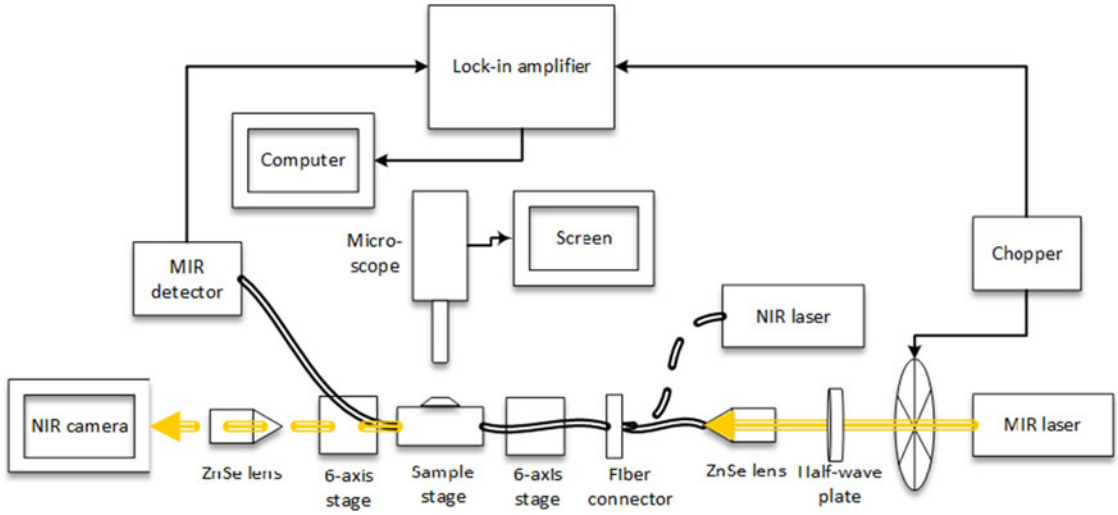

Fig. 2. Measurement setup. The dashed lines represent near-infrared light path used for visualizing waveguide mode excitation.

bends with three bending radius $r = 5\ \mu m$, 10 μm, and 25 μm are fabricated and experimentally examined. An example is shown in Fig. 1(c). The smooth and vertical sidewall will enable low loss and good waveguide performance.

The measurement setup we undertake is shown in Fig. 2. The light source is a linearly polarized continuous wave tunable laser from Daylight Solution Inc (Model TLS-41038). A half wave plate is placed right after the chopper for fine polarization control. The light is launched into the ZrF_4 mid-infrared fiber using a Thorlab fiber launch system equipped with a ZnSe focusing lens and is then butt coupled to the device sitting on the sample stage. Output light from the sample is butt coupled to another mid-infrared fiber and directed to the mid-infrared detector (Horiba DSS-IS020L) which is connected to the lock-in amplifier. Both mid-infrared fibers mentioned sit on the 6-axis stage produced by Newport. A vertical microscope above the sample stage is adopted to visualize the butt coupling condition. It is worth mentioning a 2 μm laser (Thorlab FPL2000), as well as a near-infrared camera (MicronViewer 7290A) are used for visualizing the excitation of the waveguide mode in the absence of a mid-infrared camera. The near-infrared light path is indicated by dashed lines. The output light from the sample is coupled to the near-infrared camera by another ZnSe focusing lens. It is after the inspection of waveguide mode excitation we fix the input end and change the output end to butt coupling to mid-infrared fiber.

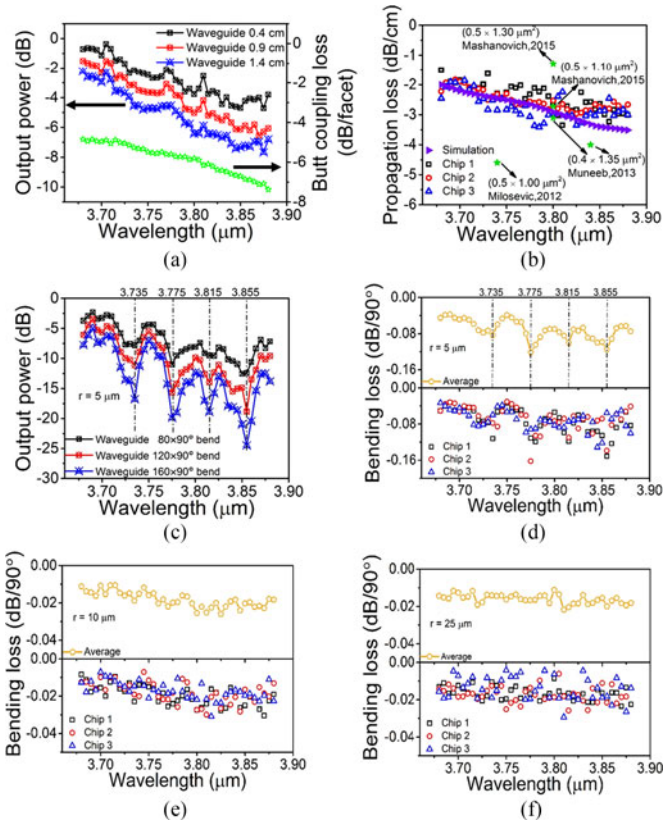

Fig. 3. (a) Averaged butt coupling loss and normalized output from a set of three cut-back waveguides for propagation loss characterization. The measured output is normalized to the fiber-to-fiber coupling output. (b) Wavelength-dependent propagation loss measured from three chips in an 8-inch wafer, together with the simulation result. The green stars show the results from the literature [13], [24], [34]. (c) Normalized output from a set of three cut-back waveguide bends with 5 μm radius. The number of 90° bend are 80, 120, and 160. (d)–(f) Wavelength-dependent bending loss of waveguide bends with (d) $r = 5$ μm, (e) 10 μm, and (f) 25 μm, from three chips in an 8-inch wafer.

Fig. 3(a) shows the wavelength-dependent averaged butt coupling loss and output power from three waveguide structures with different lengths in Chip 1 for cut-back analysis. The output power is normalized to fiber-to-fiber coupling output. The butt coupling loss increases from ~ -5 dB/facet at 3.68 μm to ~ -7.5 dB/facet at 3.88 μm. A trend of decreasing power with respect to wavelength is observed. This is the result of larger butt coupling loss and the optical mode at longer wavelength being less confined and thus more vulnerable to sidewall roughness and surrounding SiO_2 absorption. Based on the cut-back results, we numerically fit the three data points for each individual wavelength and attain the propagation loss of waveguides in Chip 1. Propagation loss results of waveguides in the other two chips are also obtained by the same method. Fig. 3(b) shows the wavelength-dependent propagation loss measured from the three chips. The propagation loss gradually increases from $\sim$2 dB/cm at 3.68 μm to $\sim$3 dB/cm at 3.88 μm as expected. Our result is comparable to previous literature shown by the green stars in Fig. 3(b). The excellent waveguide performance in the broad wavelength range could be attributed to the standard and stable process flow in the Institute of Microelectronics (IME) Singapore and the well designed waveguide that achieves strong optical mode confinement while maintaining the single mode condition.

We perform analysis on the mechanism of propagation loss in our mid-infrared waveguide. For straight waveguide, the propagation loss is attributed to scattering loss caused by sidewall roughness and absorption loss. An analytical formula to calculate sidewall roughness induced scattering loss has been proposed by Payne and Lacey [28]: $\alpha_{\max} = \frac{\sigma^2 K}{k_0 d^4 n_1}$, where α is the upper

bound of propagation loss, σ is the root-mean square surface roughness, K is a coefficient depending on waveguide geometry and the statistical distribution of surface roughness, k_0 is the wavenumber in vacuum, d is half of the waveguide width, and n_1 is the effective index of the propagating light. Assuming Gaussian distribution of surface roughness so that $K = 0.76$ and considering our waveguide dimension of 1.2 μm and the surface roughness of $\sim$5 nm achieved by IME fabrication process, we derive that the upper bound of scattering loss increases from 0.40 dB/cm at 3.68 μm to 0.44 dB/cm at 3.88 μm. Meanwhile, the absorption loss rises from 1.60 dB/cm at 3.68 μm to 3.07 dB/cm at 3.88 μm as simulated by Lumerical Mode Solution [29] (all the following simulations are performed by Lumerical Mode Solution). It is worth noting that according to *Paliks Handbook of Optical Constants of Solids* (1985) [30], the imaginary part of the refractive index (k) of Si and SiO_2 are around 1.3×10^{-8} and 4.4×10^{-5}, corresponding to the intrinsic material absorption loss of around 4.3×10^{-3} dB/cm (negligible) and 14.55 dB/cm respectively in 3.68–3.88 μm. Hence, the simulated actual loss of 1.60–3.07 dB/cm proves the strong optical mode confinement in Si rather than SiO_2. Comparing the loss contribution from the two mechanisms, we conclude that absorption loss is dominating in this mid-infrared wavelength range. The total propagation loss as a sum of scattering loss and absorption loss is plotted in Fig. 3(b), shown as purple filled triangle. Our measurement data agree well with the simulation. Although complicating the fabrication process, rib waveguide structure [31] or suspended waveguide structure [32], [33] could be adopted to lower the propagation loss for applications that require extremely low loss.

The wavelength-dependent bending loss of SOI channel waveguide bends is also characterized by the same method which has been explained in the propagation loss characterization. The results are shown in Fig. 3(c)–(f). Fig. 3(c) presents the waveguide output from a set of three cut-back waveguide bends with bending radius $r = 5$ μm. Apart from the same general trend of decreasing output power with increasing wavelength as in Fig. 3(c), four equally spaced dips located at 3.735, 3.775, 3.815, and 3.855 μm are identified with dash-dotted lines. In Fig. 3(d), the positive relationship between loss and wavelength is preserved. The average bending loss of the three chips is calculated on purpose to illustrate the oscillation of bending loss. As can be seen clearly in Fig. 3(d), the specific wavelengths where peak bending loss occur coincide perfectly with the dips in the output power from waveguide bends at 3.735, 3.775, 3.815, and 3.855 μm. The oscillation nature of the waveguide bend output and optical loss could be attributed to the Fabry-Perot cavity formed between two interfaces (see A and B in Fig. 1(c)) constructed by two connecting waveguide bends with opposite bending direction where reflection happens due to mode mismatch. The measured FSR of 0.040 μm corresponds to a Fabry-Perot cavity of length 45.1 μm which is in accordance with the physical length of 48.8 μm between interface A and B. Nevertheless, the bending loss oscillation could be eliminated by increasing the bending radius to reduce mode mismatch and hence reflection that causes Fabry-Perot cavity. As can be seen in Fig. 3(d)–(f), the oscillation is first dominating at $r = 5$ μm, then weakened at $r = 10$ μm, and becomes negligible at $r = 25$ μm. For densely integrated system where larger bends are not desired, it is suggested a straight transition waveguide is added between the two bends with opposite bending direction to reduce mode mismatch.

In $r = 5$ μm waveguide bends, the bending loss mainly distributes between 0.04–0.12 dB/90° with a gradually increasing trend (see Fig. 3(d)). In contrast, negligible increase of bending loss is observed in $r = 10$ μm and $r = 25$ μm waveguide bends. The bending loss remains at a low level between 0.01–0.03 dB/90° and 0.01–0.02 dB/90° in $r = 10$ μm (see Fig. 3(e)) and $r = 25$ μm (see Fig. 3(f)) waveguide bends, respectively. We perform simulation to examine the feasibility of further reducing the bending loss by increasing bending radius. We individually simulate the two contributions to the bending loss, namely mismatch loss and propagation loss. The results are shown in Table 1. At small bending radius ($r = 10$ μm), the mismatch loss is dominating while the propagation loss is low due to the short light propagation distance. At large bending radius ($r = 50$ μm), propagation loss starts to dominate and results in a high total loss as well. Therefore, there would exist an optimal bending radius ($r = 25$ μm) that reduces mismatch loss as much as possible while permitting a short propagating distance. The simulated losses here are lower than the measured loss since sidewall roughness is not considered.

TABLE 1
Simulation Results of Bending Loss

Radius (μm)	**10**			**25**			**50**		
Wavelength (μm)	3.68	3.78	3.88	3.68	3.78	3.88	3.68	3.78	3.88
Mismatch loss (dB/90°)	−0.012	−0.012	−0.013	−0.002	−0.002	−0.002	−0.000	−0.000	−0.001
Propagation loss (dB/90°)	−0.003	−0.004	−0.005	−0.006	−0.009	−0.012	−0.012	−0.018	−0.024
Total bending loss (dB/90°)	−0.015	−0.016	−0.018	−0.008	−0.011	−0.014	−0.012	−0.018	−0.025

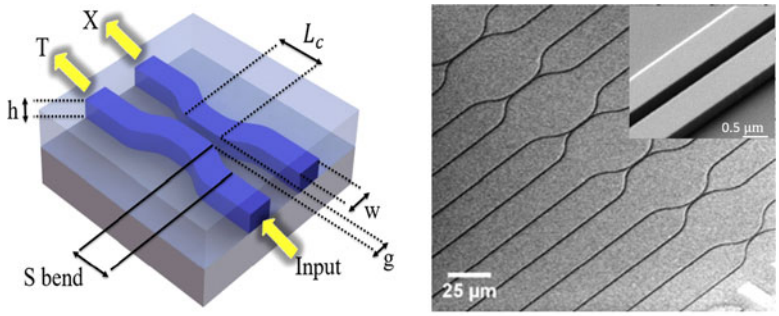

Fig. 4. (a) Schematic of the designed directional coupler for power coupling coefficient extraction. *T* and *X* are the transmitted and coupled power respectively. (b) SEM image of an array of directional couplers with varying coupling length L_c. (Inset) Zoom–in gap of a directional coupler.

Our results suggest that for waveguide bend design, the bending loss reaches a relatively saturated low value at around 0.02 dB/90° without significant oscillation when the radius is larger than 10 μm. This result is comparable to the previous success of 0.02 dB/90° bending loss in a $r = 100$ μm waveguide bend [32], but with 1/10 radius occupying only 1/100 areal footprint. Such small footprint requirement is convincing in enabling more densely integrated mid-infrared photonic circuits. The closely distributed bending loss data from the three chips show the strong credibility of the results and the device performance.

3. Directional Coupler

Fig. 4(a) shows the schematic of the designed directional coupler with labelling of the waveguide width *w*, the gap separation *g*, and the coupling length L_c. The transmitted and coupled powers are respectively labeled as *T* and *X*.

In most of the previous theoretical analysis on directional coupler, the coupled mode theory (CMT) was applied with the assumption that the two involved waveguides are close enough for evanescent coupling where S bends are not used [35]–[37]. However, most directional couplers in real-life application use S bends. In our designed directional coupler, the two waveguides are originally separated by 30 μm, then brought closely to hundreds of nanometers by S bends, and finally split again to 30 μm via S bends (see Fig. 4). Due to this fact, we slightly modify the equation obtained previously by the CMT by adding an initial phase ϕ_0 to take coupling in the S bend region

into account:

$$\frac{T}{I} = t^2 = \cos^2\left(\frac{\pi}{2}\frac{L_c}{L_\pi} + \phi_0\right) \tag{1}$$

$$\frac{X}{I} = K^2 = \sin^2\left(\frac{\pi}{2}\frac{L_c}{L_\pi} + \phi_0\right) \tag{2}$$

$$Y = \text{atan}\left(\sqrt{\frac{X}{T}}\right) = \left(\frac{\pi}{2L_\pi}\right)L_c + \phi_0. \tag{3}$$

In (1) and (2), T is the power transmitted through the waveguide where the wave is originally traveling in. X is the power coupled evanescently to the neighboring waveguide. $I = X + T$ is the total power in the directional coupler. t is the power transmission coefficient. K is the power coupling coefficient. L_c is the coupling length of the straight coupling region. L_π is the length for π phase shift as defined in the previous models without S bends [38]–[40]. ϕ_0 is the initial phase introduced by S bends. Equation (3) is derived from (1) and (2). By linear fitting Y with respect to L_c, L_π and ϕ_0 can be extracted.

For a future design guideline, we have designed three sets of devices with gap separation of 500, 550, and 600 nm, respectively. In order to extract the power coupling coefficient under each fixed gap separation, various directional couplers with different coupling lengths are designed and fabricated. Fig. 4(b) shows the SEM image of the directional couplers with various coupling lengths, while the inset shows the zoom-in gap of one of the directional couplers.

Fig. 5(a) shows the self-normalized X/I and T/I which are averaged from three chips with negligible variance. The sine squared fitting of both transmitted and coupled powers fit the data very well with adjusted R-square equal to 0.997, showing a good statistical agreement between the measured data and the analytical (1) and (2). After Y is obtained from Fig. 5(a), L_π and ϕ_0 are then extracted by the linear fitting using (3), as explained above. An example of fitting result is shown in Fig. 5(b) as inset.

The wavelength-dependent L_π is shown in Fig. 5(b). The stars represent simulated L_π. The difference of < 5 μm between the simulation and measurement result is compatible with the variance ($\sim$5 μm) of L_π measured from three chips. It is clearly revealed that L_π drops almost linearly with increasing wavelength, which agrees well with [41]. At longer wavelength, the evanescent tail of the optical mode extends further due to weaker mode confinement, leading to stronger coupling thus shorter coupling length being required to achieve the π phase shift. However, L_π is positively related to g due to more substantial evanescent tail penetration from one waveguide to the other at smaller gap separation.

Fig. 5(c) demonstrates the wavelength-dependent ϕ_0. The data is averaged from three chips with a variance of $\sim$0.05. Simulation is not performed due to the limitation of Lumerical Mode Solution. In 3.68–3.88 μm, ϕ_0 almost linearly increases, and smaller gap ($g = 500$ nm) exhibits higher ϕ_0. ϕ_0 of g = 550 nm overshoots that of $g = 500$ nm at some points due to variance caused by fabrication error. At $\lambda = 3.88$ μm, $\phi_0 = 0.207$ is achieved, showing a significant coupling caused by S bend.

The power coupling coefficient K is crucial in directional couplers with S bends since K takes ϕ_0 into account and characterizes the actual power coupling efficiency. K at $\lambda = 3.70$ μm is calculated by (2), based on the obtained L_π and ϕ_0 and presented in Fig. 5(d). As can be seen, K keeps increasing with L_c and is approaching unity. The required L_c for $K = 1$ at varying wavelength and g is plotted in Fig. 5(e). It is clear that L_c ($K = 1$) is positively related to g and negatively related to wavelength. These relations can be predicted from the previous reasoning provided to explain the dependence of L_π on g and wavelength.

Fig. 6 shows the color contour maps which are employed to visualize the dependence of power coupling coefficient K on both wavelength and L_c simultaneously. The data is averaged from three chips. The equal-K lines are slanted, indicating K is wavelength dependent. The required L_c for each wavelength to achieve three commonly used power splitting ratios, namely 50:50, 20:80, and 10:90, are marked by black, blue, and red dash-dotted lines, respectively. To demonstrate the application

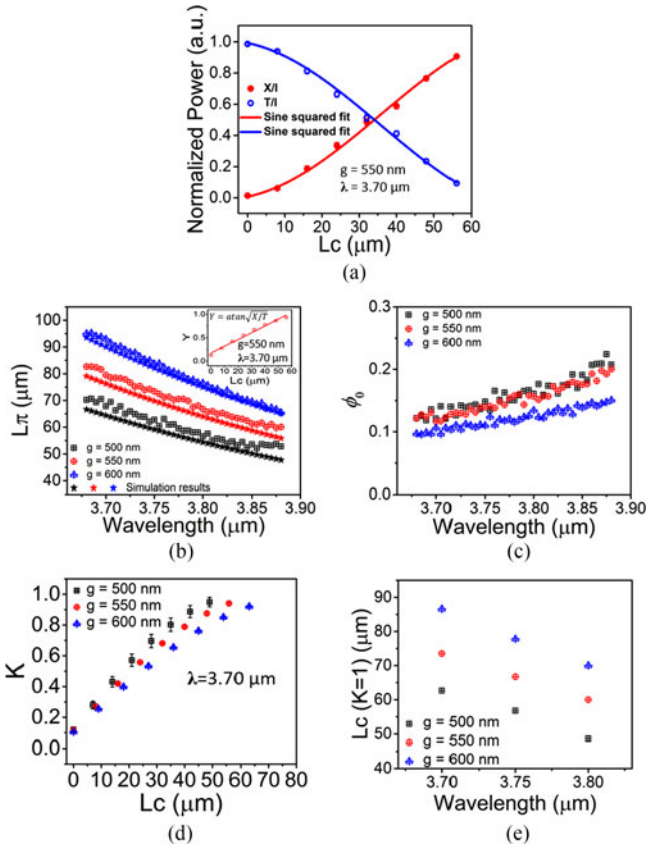

Fig. 5. (a) Self-normalized transmitted (T/I) and coupled (X/I) powers of an SOI channel waveguide directional coupler with $g = 550$ nm at $\lambda = 3.70$ μm as a function of coupling length L_c. The solid line is sine squared fit with adjusted R-square equal to 0.997. The data is averaged from three chips with negligible variance. (b) Wavelength dependent L_π of directional couplers with different gap separations g. The star symbols are the simulated L_π. (inset) Linear fitting of Y to L_c to extract L_π and ϕ_0 at 3.70 μm for the directional coupler with g = 550 nm. Extracted $L_p i$ and $_0$ are 79.48 μm and 0.173, respectively. (c) Wavelength-dependent ϕ_0. The results are averaged from three chips. (d) Power coupling coefficient K of SOI channel waveguide directional couplers with various g at 3.70 μm. (e) Required L_c for 100 % ($K = 1$) coupling at various wavelengths and g.

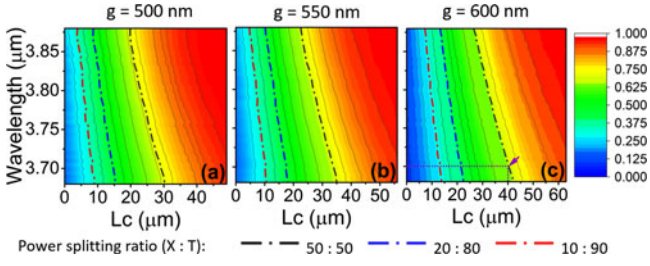

Fig. 6. Color contour maps of the dependence of K on L_c and wavelength for directional couplers with $g =$ (a) 500 nm, (b) 550 nm, and (c) 600 nm. The dash-dotted line represents three commonly used power splitting ratios '50:50,' '20:80,' and '10:90.' The purple arrow in (c) indicates the corresponding $L_c \approx 40$ μm to achieve 3 dB power splitting at 3.70 μm.

of the color contour maps and the specific power splitting ratio lines, an example is provided in Fig. 6(c). As indicated by the purple arrow, at 3.70 μm, 3 dB power splitting could be achieved by $L_c \approx 40$ μm. In a similar manner, the required coupling length L_c for any power splitting ratio could be extracted from these contour maps. This illustrates the ability of these contour maps to serve as a design guideline for mid-infrared directional couplers with arbitrary power splitting ratio.

4. Conclusion

We demonstrated SOI channel waveguide with propagation loss as low as 2 dB/cm in the broad mid-infrared range of 3.68–3.88 μm. The waveguide bending loss is as low as 0.02 dB/90° with bending radius larger than 10 μm. Our results are in accordance with the theoretical analysis and indicate the limitation of SOI waveguide loss in mid-infrared. We thoroughly investigated channel waveguide directional couplers for broadband mid-infrared applications. The power coupling coefficient for various designed directional couplers were extracted, respectively with regard to the coupling length and operation wavelength. Experimental database for directional coupler with arbitrary power splitting ratio over 200 nm bandwidth in the mid-infrared region were offered. Our result could enable novel functionalities involving evanescent coupling such as MZI and racetrack resonator for broadband mid-infrared applications.

Acknowledgment

The authors would like to thank Dr. M. Nedeljković, Dr. C. Littlejohns from Optoelectronics Research Center of University of Southampton, and Dr. C. Liu from OPTIMUS, Photonics Center of Excellence of Nanyang Technological University, for their great support on the measurement setup and data acquisition.

References

[1] F. Dell'Olio and V. M. N. Passaro, "Optical sensing by optimized silicon slot waveguides," *Opt. Exp.*, vol. 15, no. 8, pp. 4977–4993, 2007.
[2] C. A. Barrios *et al.*, "Slot-waveguide biochemical sensor," *Opt. Lett.*, vol. 32, no. 21, pp. 3080–3082, 2007.
[3] J. T. Robinson, L. Chen, and M. Lipson, "On-chip gas detection in silicon optical microcavities," *Opt. Exp.*, vol. 16, no. 6, pp. 4296–4301, 2008.
[4] C. P. Ho, B. Li, A. J. Danner, and C. Lee, "Design and modeling of 2-D photonic crystals based hexagonal triple-nano-ring resonators as biosensors," *Microsyst. Technol.*, vol. 19, no. 1, pp. 53–60, 2013.
[5] B. Li and C. Lee, "NEMS diaphragm sensors integrated with triple-nano-ring resonator," *Sensors Actuators A, Phys.*, vol. 172, no. 1, pp. 61–68, 2011.
[6] V. M. N. Passaro, B. Troia, M. L. Notte, and F. D. Leonardis, "Photonic resonant microcavities for chemical and biochemical sensing," *RSC Adv.*, vol. 3, no. 1, pp. 25–44, 2012.
[7] S. V. Singh *et al.*, "Mid-infrared materials and devices on a Si platform for optical sensing," *Sci. Technol. Adv. Mater.*, vol. 15, no. 1, 2012, Art. no. 014603.
[8] G. B. Rieker *et al.*, "Frequency-comb-based remote sensing of greenhouse gases over kilometer air paths," *Optica*, vol. 1, no. 5, pp. 290–298, 2014.
[9] G. Mi, C. Horvath, M. Aktary, and V. Van, "Silicon microring refractometric sensor for atmospheric CO_2 gas monitoring," *Opt. Exp.*, vol. 24, no. 2, pp. 1773–1780, 2016.
[10] Y. Chen, H. Lin, J. Hu, and M. Li, "Heterogeneously integrated silicon photonics for the mid-infrared and spectroscopic sensing," *ACS Nano*, vol. 8, no. 7, pp. 6955–6961, 2014.
[11] P. T. Lin *et al.*, "Chip-scale mid-infrared chemical sensors using air-clad pedestal silicon waveguides," *Lab Chip*, vol. 13, no. 11, pp. 2161–2166, 2013.
[12] P. T. Lin *et al.*, "Label-free glucose sensing using chip-scale mid-infrared integrated photonics," *Adv. Opt. Mater.*, vol. 4, no. 11, pp. 1755–1759, 2016.
[13] G. Z. Mashanovich *et al.*, "Silicon photonic waveguides and devices for near- and mid-IR applications," *IEEE J. Sel. Topics Quantum Electron.*, vol. 21, no. 4, Jul./Aug. 2015, Art. no. 2381469.
[14] Y. Zou, H. Subbaraman, S. Chakravarty, X. Xu, and A. Hosseini, "Grating-coupled silicon-on-sapphire integrated slot waveguides operating at mid-infrared wavelengths," *Opt. Lett.*, vol. 39, no. 10, pp. 3070–3073, 2014.
[15] Z. Cheng *et al.*, "Mid-infrared grating couplers for silicon-on-sapphire waveguides," *IEEE Photon. J.*, vol. 4, no. 1, pp. 104–113, Feb. 2012.
[16] P. T. Lin, V. Singh, H. Y. G. Lin, T. Tiwald, L. C. Kimerling, and A. M. Agarwal, "Low-stress silicon nitride platform for mid-infrared broadband and monolithically integrated microphotonics," *Adv. Opt. Mater.*, vol. 1, no. 10, pp. 732–739, 2013.
[17] P. T. Lin, H. Jung, L. C. Kimerling, A. Agarwal, and H. X. Tang, "Low-loss aluminium nitride thin film for mid-infrared microphotonics," *Laser Photon. Rev.*, vol. 8, no. 2, pp. 23–28, 2014.
[18] C. P. Ho, P. Pitchappa, B. W. Soon, and C. Lee, "Suspended 2-D photonic crystal aluminum nitride membrane reflector," *Opt. Exp.*, vol. 23, no. 8, pp. 10598–10603, 2015.
[19] U. Younis, S. K. Vanga, A. E. J. Lim, P. G. Q. Lo, A. A. Bettiol, and K. W. Ang, "Germanium-on-SOI waveguides for mid-infrared wavelengths," *Opt. Exp.*, vol. 24, no. 1, pp. 11987–11993, 2016.
[20] R. Soref, "Mid-infrared photonics in silicon and germanium," *Nature Photon.*, vol. 4, no. 8, pp. 495–497, 2010.
[21] R. A. Soref, S. J. Emelett, and W. R. Buchwald, "Silicon waveguided components for the long-wave infrared region," *J. Opt. A Pure Appl. Opt.*, vol. 8, no. 10, pp. 840–848, 2006.

[22] M. Nedeljkovic *et al.*, "Silicon photonic devices and platforms for the mid-infrared," *Opt. Mater. Exp.*, vol. 3, no. 9, pp. 1205–1214, 2013.
[23] J. S. Penadés, A. Z. Khokhar, M. Nedeljkovic, and G. Z. Mashanovich, "Low-loss mid-infrared SOI slot waveguides," *IEEE Photon. Technol. Lett.*, vol. 27, no. 11, pp. 1197–1199, Jun. 2015.
[24] M. M. Milošević *et al.*, "Silicon waveguides and devices for the mid-infrared," *Appl. Phys. Lett.*, vol. 101, no. 12, 2012, Art. no. 121105.
[25] X. Luo *et al.*, "Silicon-based traveling-wave photodetector array (Si-TWPDA) with parallel optical feeding," *Opt. Exp.*, vol. 22, no. 17, pp. 20020–20026, 2014.
[26] Y.-L. Cao *et al.*, "Hybrid III-V/silicon laser with laterally coupled Bragg grating," *Opt. Exp.*, vol. 23, no. 7, pp. 20020–20026, 2015.
[27] COMSOL Multiphysics Modeling Software, Mar. 1, 2017. [Online]. Available: https://www.comsol.com
[28] F. P. Payne and J. P. R. Lacey, "A theoretical analysis of scattering loss from planar optical waveguides," *Opt. Quantum Electron.*, vol. 26, no. 7, pp. 977–986, 1994.
[29] Lumerical Solutions, Inc.—Innovative Photonic Design Tools, Mar. 1, 2017. [Online]. Available: https://www.lumerical.com
[30] E. D. Palik, *Handbook of Optical Constants of Solids*. New York, NY, USA: Elsevier, 1985, pp. 547–569, 749–763.
[31] G. Z. Mashanovich *et al.*, "Low loss silicon waveguides for the mid-infrared," *Opt. Exp.*, vol. 19, no. 8, pp. 7112–7119, 2011.
[32] J. S. O. P. Enades *et al.*, "Suspended silicon mid-infrared waveguide devices with subwavelength grating metamaterial cladding," *Opt. Exp.*, vol. 24, no. 20, pp. 5661–5664, 2016.
[33] Z. Cheng, X. Chen, C. Y. Wong, K. Xu, and H. K. Tsang, "Mid-infrared suspended membrane waveguide and ring resonator on silicon-on-insulator," *IEEE Photon. J.*, vol. 4, no. 5, pp. 1510–1519, Oct. 2012.
[34] M. Muneeb *et al.*, "Demonstration of silicon-on-insulator mid-infrared spectrometers operating at 3.8 μm," *Opt. Exp.*, vol. 21, no. 10, pp. 11659–11669, 2013.
[35] A. Yariv, "Coupled-mode theory for guided-wave optics," *IEEE J. Quantum Electron.*, vol. QE-9, no. 9, pp. 919–933, Sep. 1973.
[36] A. Hardy and W. Streifer, "Coupled mode theory of parallel waveguides," *J. Lightw. Technol.*, vol. LT-3, no. 5, pp. 1135–1146, Oct. 1985.
[37] E. Marcatili, "Improved coupled-mode equations for dielectric guides," *IEEE J. Quantum Electron.*, vol. QE-22, no. 6, pp. 988–993, Jun. 1986.
[38] R. R. A. Syms and J. R. Cozens, *Optical Guided Waves and Devices*. Berkshire, U.K.: McGraw-Hill, 1992, pp. 243–250.
[39] K. Okamoto, *Fundamentals of Optical Waveguides*. London, U.K.: Elsevier, 2002, pp. 159–168.
[40] R. G. Hunsperger, *Integrated Optics-Theory and Technology*. New York, NY, USA: Springer, 2009, pp. 153–160.
[41] M. Stegmaier and W. H. P. Pernice, "Broadband directional coupling in aluminum nitride nanophotonic circuits," *Opt. Exp.*, vol. 21, no. 6, pp. 7304–7315, 2013.